Supporting information for "Vacuum Ultraviolet Light-Generating Metasurface"

*Michael Semmlinger,[1,2] Ming Lun Tseng,[3,4] Jian Yang,[2,5] Ming Zhang,[2,5] Chao Zhang,[1,2] Wei-Yi Tsai,[3,4] Din Ping Tsai,[3,4] Peter Nordlander,[1,2,5] and Naomi J. Halas[1,2,5,6]**

[1]Department of Electrical and Computer Engineering, Rice University, Houston, Texas 77005, United States.

[2]Laboratory for Nanophotonics, Rice University, Houston, Texas 77005, United States.

[3]Research Center for Applied Sciences, Academia Sinica, Taipei 115, Taiwan.

[4]Department of Physics, National Taiwan University, Taipei 10617, Taiwan.

[5]Department of Physics and Astronomy, Rice University, Houston, Texas 77005, United States.

[6]Department of Chemistry, Rice University, Houston, Texas 77005, United States.

*Corresponding Author: Naomi J. Halas, E-mail: halas@rice.edu

Section S1. Choice of nonlinear material

Selecting the right base material is crucial in the design of a nonlinear metasurface capable of efficient VUV light generation. Two important principles need to be considered: The material should be lossless and have a high refractive index at the fundamental wavelength (394 nm) to achieve strong light-matter interactions in subwavelength meta-atoms[1]. For example, germanium[2] and silicon[3] and have been used in the fabrication of all-dielectric metasurfaces for harmonic generation from the near-IR to the visible. However, their relatively high optical losses in the visible make them unsuitable for nonlinear metasurfaces in this wavelength regime. ZnO has both a high refractive index, as well as near-zero extinction coefficient (k~0) at the fundamental wavelength, and is therefore a well suited material. ZnO can be efficiently prepared by conventional methods such as sputtering and chemical synthesis, making it promising for applications in nonlinear devices. In this work, sputtered ZnO films on glass or fused silica substrates were purchased from MTI corporation, USA (Item Numbers: ZnO on Glass -252507-150nm and ZnO on Fused Silica -101005-100nm).

Section S2. Experimental measurements and data analysis

2.1 Linear measurements

The linear transmission measurements were performed with a standard spectroscopy setup (Figure S1). A laser driven white light source (Energetic LDLS) was used for excitation. A specific wavelength was selected with a scanning monochromator (Princeton Instruments Action SP2150) that utilized a 1200 groves/mm grating. After passing through a polarizer, the beam passed through a diffuser to increase uniformity, and was focused on the sample via a fused silica lens with a focal length of 40 mm. The transmitted beam passed the sample from the substrate side, was then collected with a reflective objective (Edmunds Optics, 15x/0.28), and finally focused onto a hyperspectral CCD camera (Princeton Instruments PIXIS 1024). The wavelength was stepped in increments of 2 nm. The relative transmission

spectra were then obtained by dividing the collected data from the sample, by that of the adjacent un-patterned substrate.

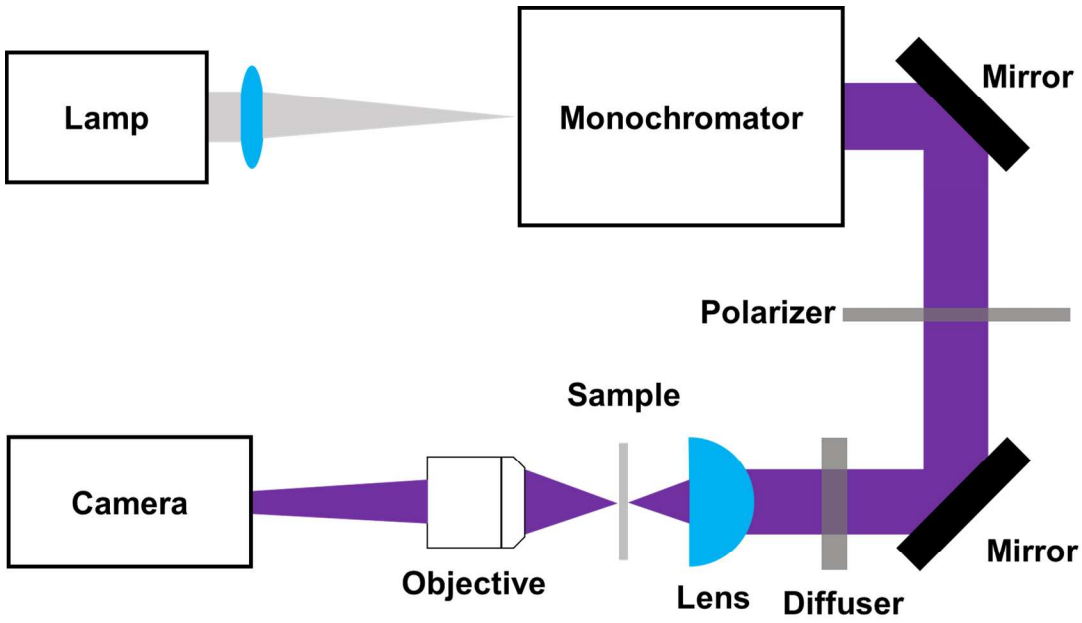

Figure S1. Experimental setup for relative transmission measurements.

2.2 Nonlinear measurements

For general information about the setup for spectral scans shown in Figure S2, please see the Methods section in the main text. The monochromator was calibrated using the high energy spectrum from a white light source (blue side of the visible and near UV light). A calibration lamp (Newport, Hg(Ne)) was used to verify that the calibration accurately predicted the correct wavelengths in the relevant wavelength regime. At each wavelength increment, five measurements of the PMT current and the average laser power were performed. First, the dark values were subtracted. Second, the current values were normalized by dividing by the power values squared. Finally, the five points were averaged.

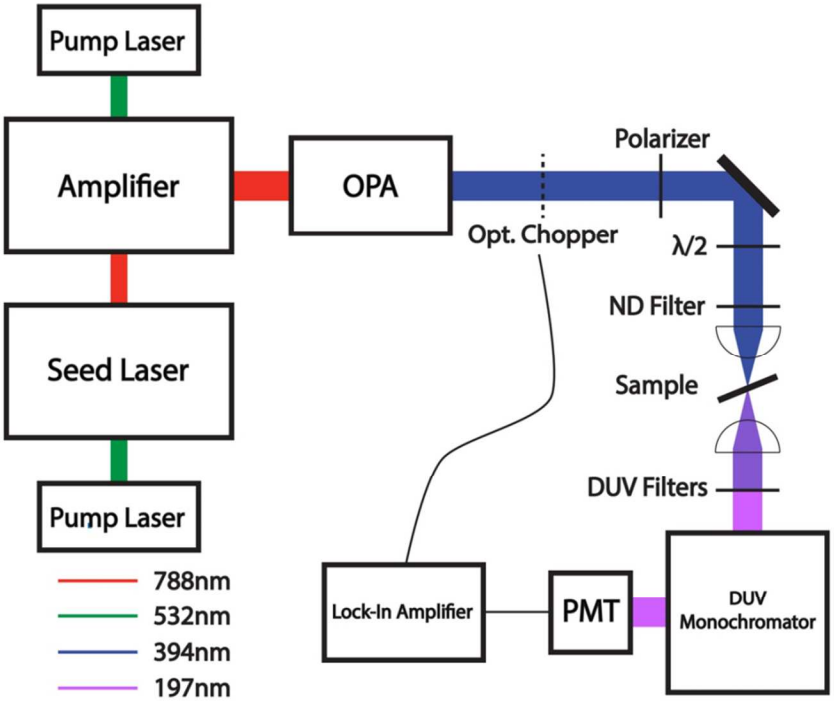

Figure S2. Experimental setup for SHG spectral scans.

For all non-spectral measurements, including power and angle scans (change in incident angle ϕ, measured from normal), a simplified measurement setup was used (Figure S3A). Note that minimal optics were used in the power dependence measurements to avoid any extra effects. Three bandpass filters were used to separate out the second harmonic (SH) signal instead of using a monochromator. The PMT was a Thorlabs PMTSS in this case. This simplified setup only used minimal optics which is not only convenient in operation but has the additional advantage that the attenuation of the SH signal by the optical components can be easily adjusted for in calculations, making it possible to accurately determine the conversion efficiency. In addition, a shorter path length also helps minimizes absorption of the SH signal in air. To compensate for any remaining fundamental signal, measurements with a glass slide which acts as a long pass filter that blocks the SH signal (Figure S4B) were performed.

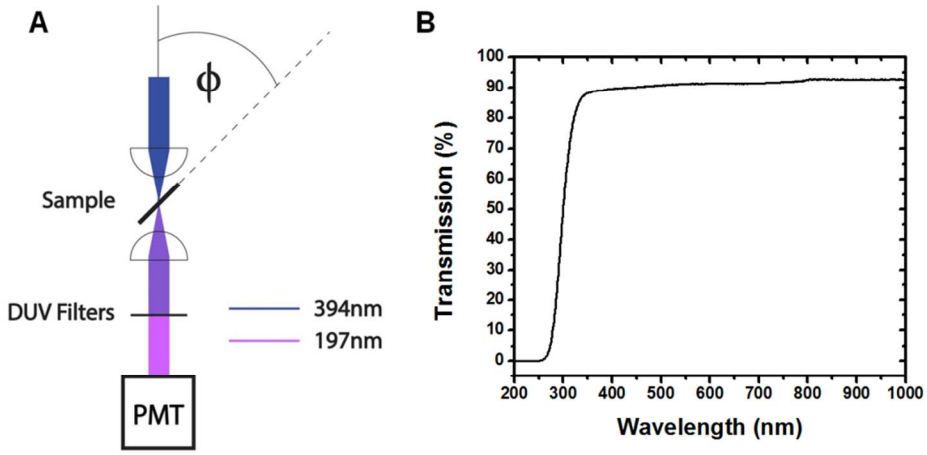

Figure S3. Simplified experimental setup for SHG measurements. (A) Setup for non-spectral scans. (B) Transmission spectrum of the glass slide.

2.3 Data analysis

The measured PMT current data was analyzed as follows. At each data point ten measurements of the PMT current and the average laser power were taken immediately after one another. First, the dark values were subtracted. Second, the ten points were averaged. Third, the PMT current measurements with the longpass filter were subtracted from the ones without (the transmission of the glass was also compensated for). For power measurements these values were then plotted, where the peak power density was estimated based on the spot size, the pulse width and repetition rate of the laser. The conversion efficiency was estimated by taking into account the sensitivity of the PMT, as well as the transmission values of all relevant optical components. For the angle scan in Figure S4, the data was analyzed using the same three steps described above, but in addition the current values were normalized by dividing by the power values squared. The effective nonlinear coefficient was calculated using the formula provided in the main text. Within the points 0.042 mW to 0.196 mW, the average nonlinear coefficient is 0.96 pm/V. For lager powers (0.226 mW to 1.682 mW), where deviation from the quadratic power dependence can be observed, the average coefficient drops to 0.66 pm/V.

Section S3. Incident angle dependence

Figure 3b in the main text shows the incident angle dependence of both the sample and the thin film. For our sample, we see a SHG signal intensity peak at 7°. To understand the incident angle dependence line shape, two factors need to be considered: symmetry breaking and resonance shifting. When the pump beam deviates from normal incidence, asymmetry is introduced and causes more constructive interference across the nanoresonator at the SHG wavelength. We attribute the increasing trend at high angles (from 10 to 12°) to the increased symmetry breaking, while the transmission resonance shifting causes the peak at 7°. This can be shown in simulation that the transmission resonance due to the magnetic mode red shifts with increasing incident angle (Figure S4). Figure S4 shows that for an incident angle between 9 and 12 deg, the resonance shifts to our fundamental wavelength 394nm. This is in relatively good agreement with our experimentally measured maximum at 7 deg. Since the SHG intensity is very sensitive to field enhancement, this slight resonance shift could play a big role. Both factors combine to produce our observed incident angle dependence line shape.

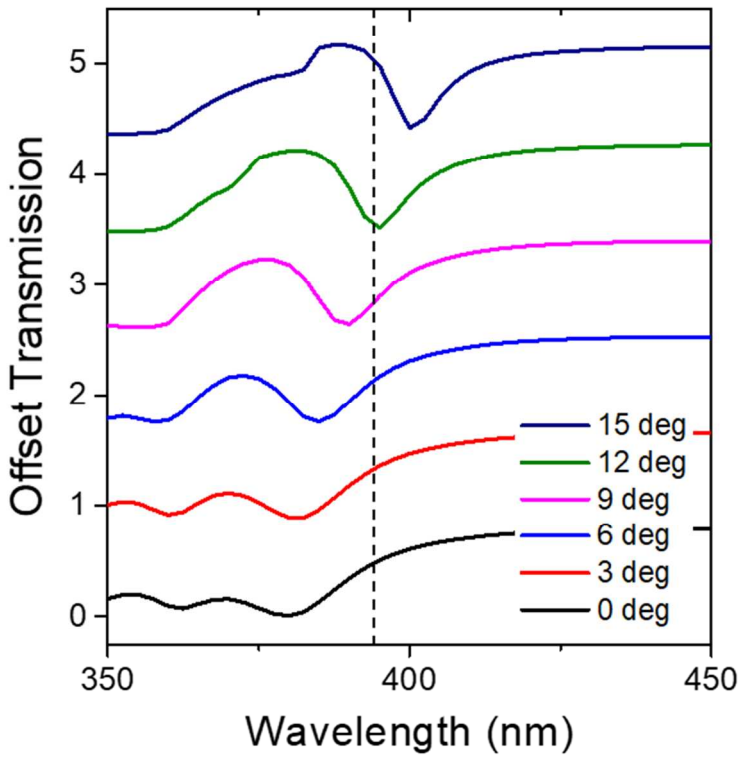

Figure S4. Simulated transmission spectra at different incident angles. The dashed line indicates the excitation wavelength.

Section S4. Device stability

Figure S5 shows that our metasurface exhibits good stability under continuous exposure. For this experiment a similar, but not identical device to the one reported in the main text was used. The ZnO disks had a diameter of 185 nm, with periods P_x = 245 nm and P_y = 245 nm. The ZnO thickness was 100 nm, on a silica substrate. A 3 nm Cr layer was added for conduction. In the experiment, data points were taken about every 30 s for one hour. The simplified setup (Figure S3A) was used. A dark measurement was taken initially and subtracted from each data point, as well as a measurement with a longpass filter that was subtracted proportionally. The experiment was performed under normal incidence.

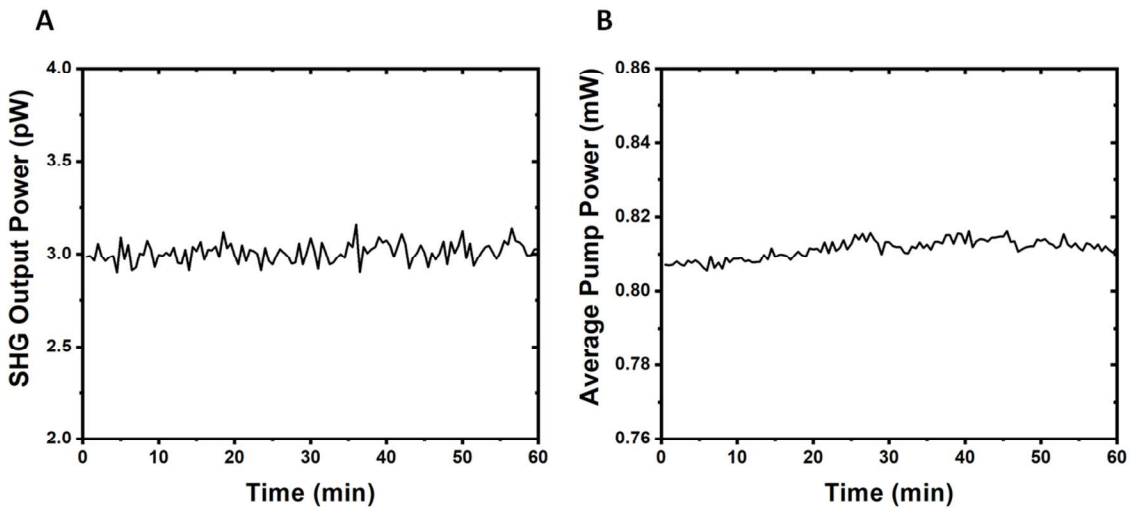

Figure S5. Device stability. (A) The SHG output power and (B) corresponding average pump power are plotted with respect to time. The measurement increments are 30 s.

Section S5. Polarization of the SH signal

In the following we present a short theoretical analysis of the polarization of the SHG signal from a ZnO thin film as well as the metasurface discussed in this work. The 6 mm symmetry of the ZnO wurtzite crystal structure supports five nonzero elements of the second order nonlinear susceptibility tensor (written in d matrix notation):

$$d = \epsilon_0 \begin{pmatrix} 0 & 0 & 0 & 0 & d_{15} & 0 \\ 0 & 0 & 0 & d_{24} & 0 & 0 \\ d_{31} & d_{32} & d_{33} & 0 & 0 & 0 \end{pmatrix}$$

Therefore, for the thin film under p-polarized excitation, the incident field has components E_x and E_z, and the nonlinear polarization will also be p-polarized:

$$P_x(2\omega) = 4d_{15}\epsilon_0 E_x(\omega)E_z(\omega)$$

$$P_z(2\omega) = 2d_{31}\epsilon_0 E_x(\omega)^2 + 2d_{33}\epsilon_0 E_z(\omega)^2$$

Under s-polarized excitation, the incident field only has the component E_y; so the nonlinear polarization will be in z direction:

$$P_z(2\omega) = 2d_{32}\epsilon_0 E_y(\omega)^2$$

The nonlinear signal will also be p-polarized in this case, but the signal will be much lower compared with p-polarized excitation. Therefore, it can be concluded that the nonlinear signal will be p-polarized regardless of the polarization of the input signal (Figure S6). This is confirmed by the polarization measurements reported by other groups in which ZnO thin films were used for SHG from the infrared to the visible [4, 5].

Compared to the thin film, the metasurface reported in this work shows a more complex field distribution at the fundamental frequency due to the magnetic dipole mode. However, similar conclusions can be reached through similar analysis.

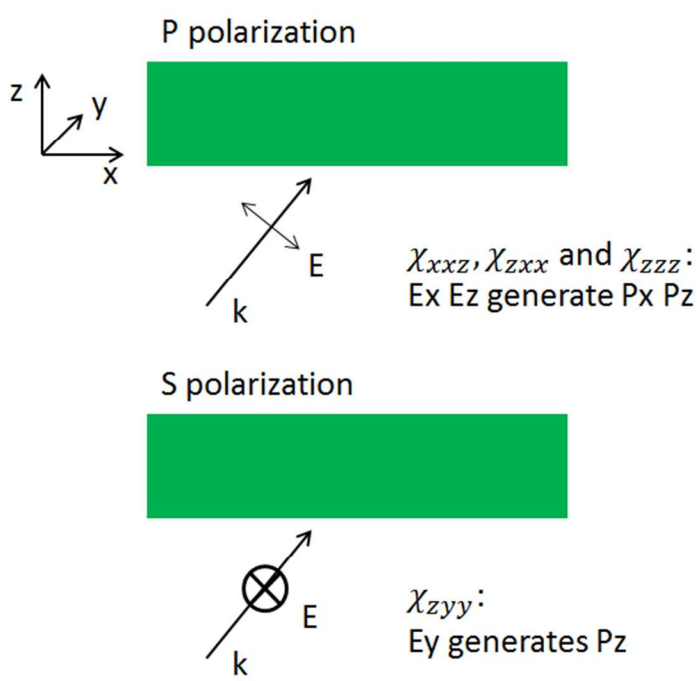

Figure S6. Theoretical prediction of the polarization of the SH signal.

Section S6. Absorption in the chromium layer

Due the lossy nature of Cr at the SHG frequency, the thin Cr layer on the top of the metasurface may cause an extra loss of the SHG signal. Our simulations indicate that for a ZnO thin film, a SH signal reduction of 75% is expected. However, in our simulations we found that the linear and nonlinear response of the metasurface is not strongly affected by the Cr layer (Figure S7). This is probably because the resonance mode at the fundamental and the field distribution at the doubled frequency are predominantly confined inside and on the side walls of the disk instead of on its top surface. It can be noted that this is quite different from plasmonic resonances, in which all field enhancement is generally located at the top/bottom surface and/or outside the nanostructures.

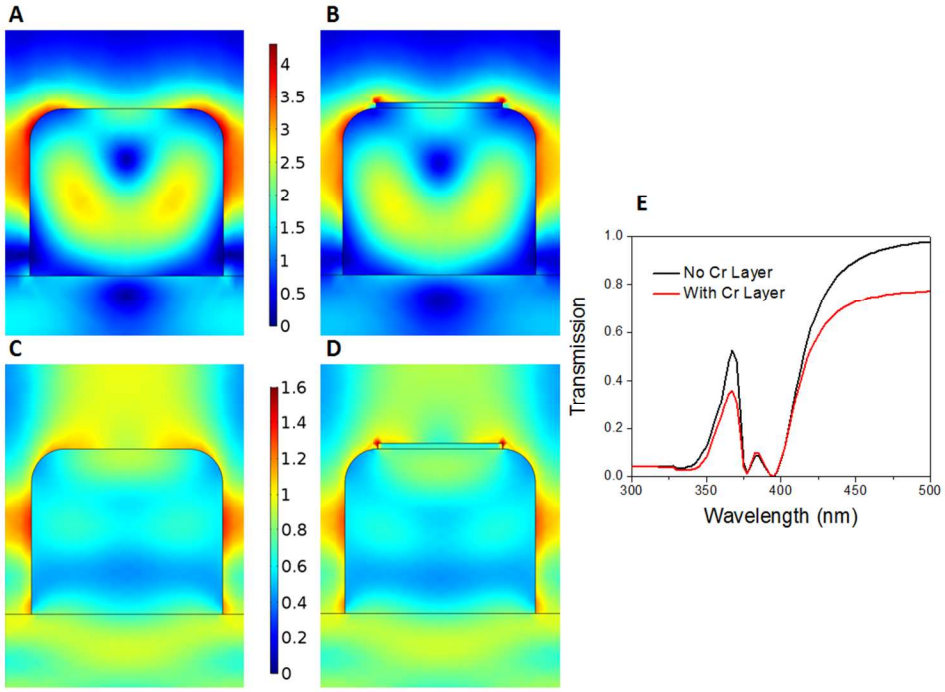

Figure S7. Theoretical study on the influence of the Cr layer. Electric field profile is plotted at the fundamental wavelength (394 nm) (A) without and (B) with the Cr layer, and at the SHG wavelength (197 nm) (C) without and (D) with the Cr layer. (E) Transmission spectrum without and with the Cr layer.

Section S7. Radiation pattern

The magnetic dipole sample used for the radiation pattern experiment consists of an array of disked shaped ZnO nanoresonators. However, the diameter and the periods are larger (see main text), so that the radiation pattern can be readily captured. For completeness we would also like to mention that there were some other minor differences to the sample used for the previous measurements. While for the latter we used a 150 nm thick ZnO thin film on a glass substrate to cut out the metasurface, for the former we used a 100 nm ZnO thin film on a fused silica substrate. For the radiation pattern sample the Cr layer was also reduced from 5 nm to 3 nm. For the radiation pattern imaging we used a simplified setup, similar to Figure S3a. However, instead of a PMT, we now used a CCD camera (Princeton Instruments PIXIS 1024BUV) as a detector. An integration time of 1000 s was used. An additional bandpass filter was added (four total) to reduce the exposure from the fundamental signal. Figure S8A shows the radiation pattern image from Figure 4a in the main text, but not plotted with a color map and without the cover over the center. Figure S8B) shows the results from a similar measurement was taken with a glass slide which acts as a longpass filter (Figure S8B) in the path. This confirms that the diffraction pattern comes from the SH signal.

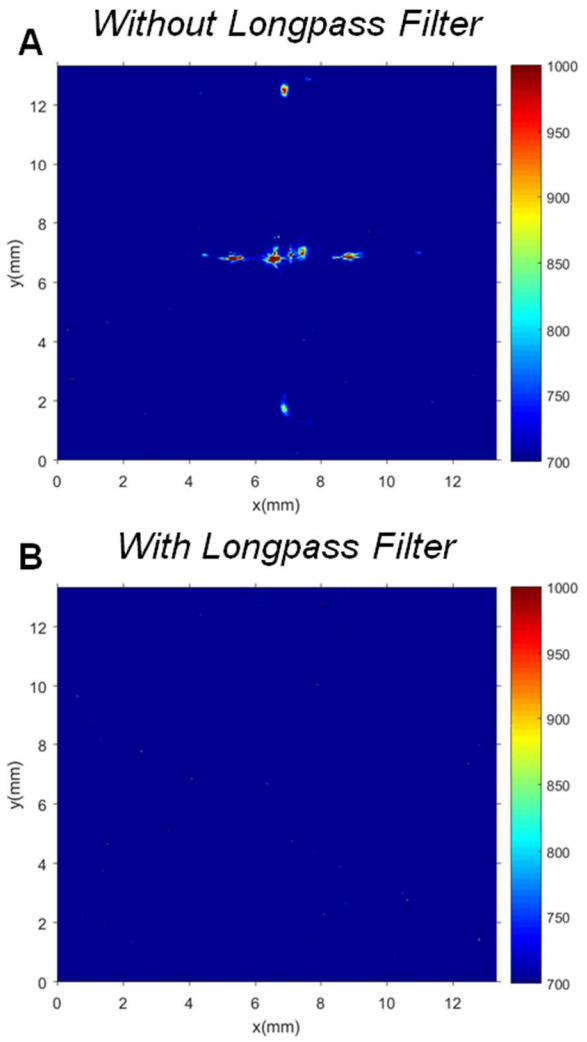

Figure S8. Radiation pattern images as color map plots. (A) Without and (B) with a longpass filter.

We also investigated theoretically how to manipulate radiation pattern by changing our sample design. Figure S9A shows the simulated diffraction pattern of a metasurface with D = 390 nm, P_x =650 nm, P_y = 450 nm, with a large range of angles. Figure S9B shows that we can manipulate the emission angles by changing the lattice constants of our sample. Furthermore, if we introduce symmetry breaking into our unit cells by using half-disks, we can adjust the relative intensities between different diffraction orders (Figure S9C).

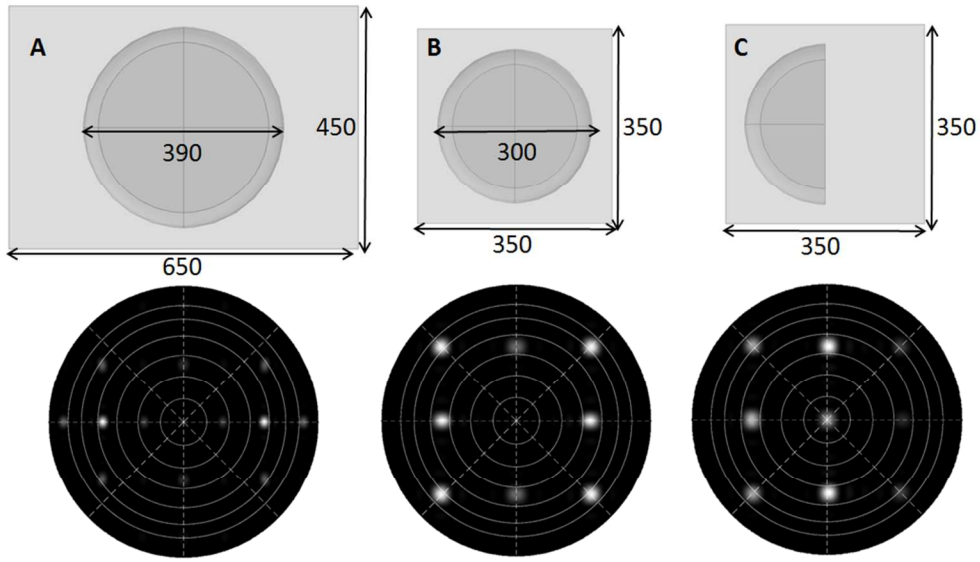

Figure S9. Theoretical study on manipulation of the SH signal. By tuning the lattice constants and introducing symmetry into the unit cells, we can adjust the spacing and relative intensities of different diffraction orders.

Section S8. Discussion on the origin of the saturation effect in power dependence measurement

The saturation effect in the power dependence can in principal result from several mechanisms such as local heating from ZnO defects and multiphoton absorption (in the metasurface layer or the substrate). To address this issue, we performed calculations to estimate the influence of two-photon absorption in the ZnO metasurface and the glass substrate following the method provided in the main text Ref. [15]. The two-photon absorption coefficients for ZnO and glass were adopted from Ref. [6] and Ref. [7] in the Supporting Information, respectively. The estimated values based on these calculations were around 1mm and 3cm for ZnO and glass, respectively. The calculated penetration depths are much larger than the thicknesses of the materials used in this work (150nm for ZnO and 0.7mm for the glass substrate). While the excitation wavelengths in the reported references that we were able to find are somewhat different from ours, we believe they are sufficient for an order of magnitude estimation. Considering this, we find it unlikely that multiphoton absorption effects play a significant role in the saturation

effect. Instead, we attribute it to local heating of the defects in the metasurface layer under high laser power illumination. This was also observed in a previous work reported in the main text Ref. [16].

References for supporting information

1. Jahani, S.; Jacob, Z. *Nat Nano* **2016,** 11, (1), 23-36.
2. Grinblat, G.; Li, Y.; Nielsen, M. P.; Oulton, R. F.; Maier, S. A. *Nano Lett.* **2016,** 16, (7), 4635-40.
3. Yang, Y.; Wang, W.; Boulesbaa, A.; Kravchenko, II; Briggs, D. P.; Puretzky, A.; Geohegan, D.; Valentine, J. *Nano Lett.* **2015,** 15, (11), 7388-93.
4. Cao, H.; Wu, J. Y.; Ong, H. C.; Dai, J. Y.; Chang, R. P. H. *Appl. Phys. Lett.* **1998,** 73, (5), 572-574.
5. Liu, C. Y.; Zhang, B. P.; Binh, N. T.; Segawa, Y. *Optics Communications* **2004,** 237, (1), 65-70.
6. Vivas, M. G.; Shih, T.; Voss, T.; Mazur, E.; Mendonca, C. R. *Opt. Express* **2010,** 18, (9), 9628-9633.
7. Mizunami, T.; Takagi, K. *Opt. Lett.* **1994,** 19, (7), 463-465.